CrossMark

ORIGINAL PAPER

Rapid pre-eruptive thermal rejuvenation in a large silicic magma body: the case of the Masonic Park Tuff, Southern Rocky Mountain volcanic field, CO, USA

J. T. Sliwinski[1] · O. Bachmann[1] · M. A. Dungan[2] · C. Huber[3] · C. D. Deering[4] ·
P. W. Lipman[5] · L. H. J. Martin[1] · C. Liebske[1]

Abstract Determining the mechanisms involved in generating large-volume eruptions (>100 km^3) of silicic magma with crystallinities approaching rheological lock-up (~50 vol% crystals) remains a challenge for volcanologists. The Cenozoic Southern Rocky Mountain volcanic field, in Colorado and northernmost New Mexico, USA, produced ten such crystal-rich ignimbrites within 3 m.y. This work focuses on the 28.7 Ma Masonic Park Tuff, a dacitic (~62–65 wt% SiO$_2$) ignimbrite with an estimated erupted volume of ~500 km^3 and an average of ~45 vol% crystals. Near-absence of quartz, titanite, and sanidine, pronounced An-rich spikes near the rims of plagioclase, and reverse zoning in clinopyroxene record the reheating (from ~750 to >800 °C) of an upper crustal mush in response to hotter recharge from below. Zircon U–Pb ages suggest prolonged magmatic residence, while Yb/Dy vs temperature trends indicate co-crystallization with titanite which was later resorbed. High Sr, Ba, and Ti concentrations in plagioclase microlites and phenocryst rims require in-situ

feldspar melting and concurrent, but limited, mass addition provided by the recharge, likely in the form of a melt-gas mixture. The larger Fish Canyon Tuff, which erupted from the same location ~0.7 m.y. later, also underwent pre-eruptive reheating and partial melting of quartz, titanite, and feldspars in a long-lived upper crustal mush following the underplating of hotter magma. The Fish Canyon Tuff, however, records cooler pre-eruptive temperatures (~710–760 °C) and a mineral assemblage indicative of higher magmatic water contents (abundant resorbed sanidine and quartz, euhedral amphibole and titanite, and absence of pyroxene). These similar pre-eruptive mush-reactivation histories, despite differing mineral assemblages and pre-eruptive temperatures, indicate that thermal rejuvenation is a key step in the eruption of crystal-rich silicic volcanics over a wide range of conditions.

Keywords Silicic magma · Ignimbrite · Plagioclase zoning · Self-mixing · Rejuvenation · Zircon

✉ J. T. Sliwinski
jakub.sliwinski@erdw.ethz.ch

1 ETH Zürich, 8092 Zurich, Switzerland

2 University of Oregon, Eugene, OR 97403-1272, USA

3 Brown University, Providence, RI 02912, USA

4 Michigan Technological University, Houghton, MI 49931, USA

5 US Geological Survey, Menlo Park, CA 94028, USA

Introduction

Understanding the eruption mechanism(s) for large silicic magma bodies (>100 km^3) with crystallinities close to the rheological locking point (~50 vol%, e.g., Marsh 1981) is a long-standing problem, as the high effective viscosities of such magmas appear to make them nearly uneruptible (Marsh 1981; Scaillet et al. 1998; e.g.; Gottsmann et al. 2009). Magmas with such high crystallinities have been described as: "a mixture of crystals and silicate liquid whose mobility, and hence eruptibility, is inhibited by a high fraction of solid particles" (Miller and Wark 2008). A potential mechanism for creating the necessary conditions for the eruption of massive volumes of crystal-rich magma

🖄 Springer

is reheating and partial melting of shallow-seated crystal mushes, which makes them less viscous and increases the internal overpressure of the reservoir (e.g., "Mush defrosting" of Mahood 1990; see also Murphy et al. 2000; Bachmann et al. 2002; Huber et al. 2012; Klemetti and Clynne 2014; Kaiser et al. 2016; Bachmann and Huber 2016). Such models require that significant volumes of hotter recharge occur periodically, while large (100's to 1000's km^3) mushes remain above their solidi, potentially for long periods of time (>thousands of years). Effects of recharge and longevity of mushes remain controversial, both on the basis of thermal models (Annen 2009; Huber et al. 2009, 2011; Gelman et al. 2013; Gutierrez et al. 2013) and geochronological studies (e.g., Reid et al. 1997; Brown and Fletcher 1999; Schmitt et al. 2003; Vazquez and Reid 2004; Charlier et al. 2005; Bachmann et al. 2007; Crowley et al. 2007; Walker et al. 2007; Simon et al. 2008; Claiborne et al. 2010; Tappa et al. 2011; Schoene et al. 2012; Storm et al. 2012; Zimmerer and McIntosh 2012; Cooper and Kent 2014; Barboni et al. 2016). Hence, further testing of the mush rejuvenation model under different conditions and settings is important for elucidating the thermo-mechanical behavior of magmas in large upper crustal reservoirs.

This paper focuses on compositional variations, mineral textures, and mineral chemistry of the ~500 km^3 Masonic Park Tuff (MPT), a "monotonous intermediate" (unzoned, crystal-rich dacitic ignimbrite; Hildreth 1981) that was erupted ~28.7 Ma in the Southern Rocky Mountain volcanic field (SRMVF). Textural manifestations of disequilibrium in most minerals, in combination with complex mineral zoning patterns, are consistent with magma injection and mixing prior to eruption and a role for recharge in triggering the eruption. The MPT is compared to the archetypal monotonous intermediate that erupted in the same area—the 28.02-Ma Fish Canyon Tuff (FCT, all previously published ages adjusted to this age), which also was thermally rejuvenated prior to eruption (Bachmann and Dungan 2002; Bachmann et al. 2002). We highlight the many similarities and striking differences between these units as a means of constraining the range of conditions necessary for eruption of voluminous, crystal-rich magmas from upper crustal reservoirs.

Geological setting

The SRMVF, a large-volume continental-arc province in Colorado and northern New Mexico, is the source of 28 large caldera-forming ignimbrites in Colorado and northern New Mexico and a manifestation of subduction along the North American margin in the Cenozoic (Fig. 1; Lipman et al. 1978; Lipman 2000, 2007; Lipman and Bachmann 2015). The SRMVF and, more specifically, its largest

erosional remnant preserved in the San Juan Mountains represent an exceptional natural laboratory for understanding the processes responsible for the generation of large quantities of diverse evolved magmas. Mountainous terrain and variable erosion provide three-dimensional exposures of most units. Meanwhile, recurrent caldera sources are spatially clustered, and repose times between large eruptions of magmas generated from the same crustal column are relatively brief.

Initial volcanism in the San Juan region (~34.5–30.1 Ma), the Conejos Formation (e.g., Zielinsky and Lipman 1976; Colucci et al. 1991; Lipman 2007), was dominantly andesitic and primarily constructed large stratovolcanoes. More silicic magmas (dacite to rhyolite) began to erupt as large ignimbrites and associated calderas (reviewed by Lipman 2000, 2007) at about 30.1 Ma. The loci of ignimbrite-forming eruptions migrated from the southeast and west towards the central San Juan caldera cluster about 28.7 Ma (Steven and Lipman 1976), and this cluster became the primary locus of activity. Andesitic lavas continued to erupt within and around the peripheries of many of these calderas throughout the period of ignimbrite generation. This was the dominant mode of regional volcanism until the decline of subduction-related activity at ~26.5 Ma (mid-Tertiary ignimbrite flare-up; see Lipman and McIntosh 2008).

The extremely productive central San Juan caldera cluster (Lipman 2006) erupted nine large ignimbrites in less than 2 Myr (Lipman and McIntosh 2008); four are compositionally zoned (crystal-poor rhyolite to crystal-rich dacite), and five are homogeneous crystal-rich dacites. The oldest of these, the Masonic Park Tuff (MPT), is the focus of this study. Its erupted volume is roughly estimated at ~500 km^3, sufficiently large that a caldera source seems required. Its eruption age is 28.7 Ma based on $^{40}Ar/^{39}Ar$ biotite and sanidine ages of bracketing tuffs (Lipman and McIntosh 2008; Lipman and Bachmann 2015). This ignimbrite overlies intermediate-composition lavas of the Conejos Formation and the 28.75-Ma South Fork Tuff (Platoro caldera; Lipman et al. 1996); it is overlain by the 28.58-Ma Chiquito Peak Tuff within a narrow areal overlap zone along paleo-drainages proximal to present-day South Fork, CO. MPT exposures are limited to the proximal periphery of the southern La Garita caldera, the source of the far more voluminous FCT, suggesting that the MPT caldera source lies buried within the central San Juan cluster.

West of South Fork, MPT is widely overlain by FCT, except in a zone adjacent to the southeast margin of the La Garita caldera, where lavas of Sheep Mountain Andesite (SMA) intervene between the MPT and FCT. The SMA (Lipman et al. 1996; Lipman 2000) is relatively thin in these presumably distal remnants and its vent region is inferred to have been in the MPT source within the southern
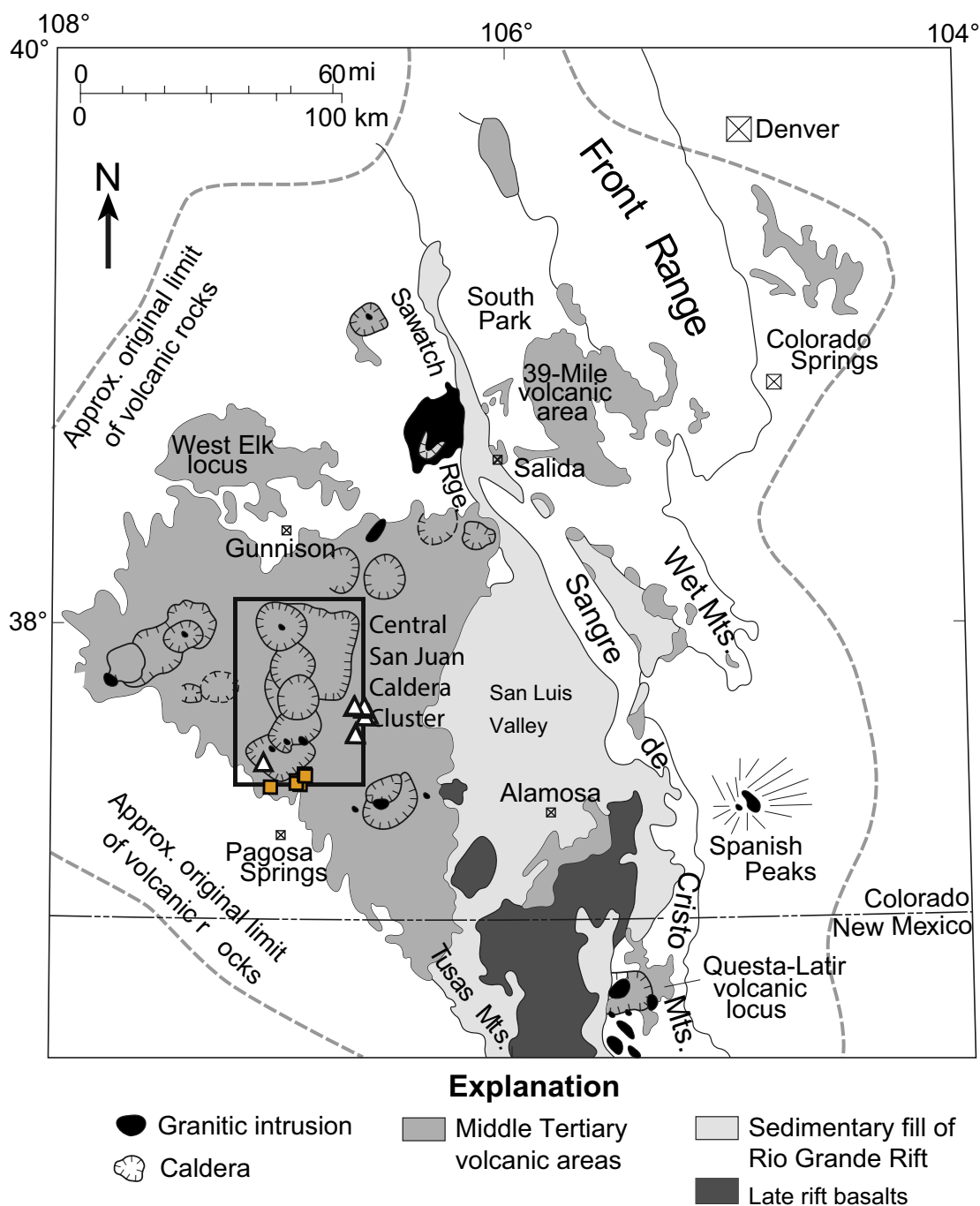
Explanation

● Granitic intrusion   ▨ Middle Tertiary volcanic areas   ▢ Sedimentary fill of Rio Grande Rift

🜄 Caldera   ▨ Late rift basalts

Fig. 1 Simplified map of the Southern Rocky Mountain volcanic field (*gray shaded areas*), showing location of the San Juan erosional remnant. *Black box*, central San Juan caldera cluster. Map modified from Lipman (2007). *Triangles* denote MPT sampling locations from this study and previous studies (see Appendix); *orange squares* denote Sheep Mountain Andesite sampling locations from previous studies. For more detailed map, see Lipman (2006)

La Garita caldera. Its original eruptive volume was likely more substantial than the preserved volume. The close timing of the SMA and MPT eruptions is documented by the locally overlying Chiquito Peak Tuff (28.58 Ma). The SMA is one of many postcaldera intermediate lava sequences in the San Juan region that demonstrates a quasi-continuous caldera-centric input of magma that was hotter and less evolved than the tuffs erupted during caldera-forming events; e.g., post-FCT Huerto Andesite (Parat et al. 2005; Lipman 2007).

Table 1 Whole-rock analyses of MPT bulk tuff

Sample No.	95L-10	93L-5A	93L-9B	93L-11A	93L-13B	MAD-240	MAD-240A	MAD241	LR89-003	LR89-005	MPT08-1C	MPT08-1D	MPT08-2EA	MPT08-7
Source	L96	L96	L96	L96	L96	L96	L96	L96	R91	R91	TS	TS	TS	TS
SiO_2	60.92	67.37	61.57	61.48	64.3	63.06	63.08	61.25	61.88	62.14	63.27	62.48	63.26	61.32
TiO_2	0.84	0.67	0.81	0.81	0.75	0.77	0.77	0.83	0.80	0.77	0.76	0.74	0.79	0.80
Al_2O_3	16.78	13.39	16.06	16.24	15.37	15.97	16.00	16.35	15.82	16.10	15.56	14.96	14.94	15.95
$Fe_2O_3^T$	6.41	4.94	6.52	6.33	5.54	5.59	5.59	6.47	6.53	6.73	5.73	5.45	6.41	6.40
MgO	2.07	1.43	2.28	2.28	1.99	1.81	1.86	2.46	1.87	2.00	1.64	1.65	1.89	2.36
CaO	4.87	4.28	4.38	4.82	4.99	4.66	4.58	4.62	4.48	4.64	4.27	5.42	4.09	4.75
Na_2O	3.54	2.61	3.34	3.42	2.63	3.50	3.51	3.50	3.49	3.52	3.41	3.31	3.30	3.89
K_2O	3.29	3.65	3.74	3.58	3.14	3.49	3.51	3.49	3.76	3.49	3.72	3.92	3.97	2.77
P_2O_5	0.33	0.33	0.34	0.36	0.33	0.33	0.33	0.34	0.30	0.30	0.29	0.28	0.30	0.31
MnO	0.08	0.06	0.10	0.10	0.07	0.09	0.09	0.08	0.10	0.10	0.09	0.13	0.09	0.12
LOI	1.85	2.16	2.20	2.07	3.70	0.41	0.60	1.54	0.79	0.41	1.26	1.68	0.97	1.33
Total	99.15	98.74	99.14	99.42	99.11	99.28	99.33	99.40	99.03	99.79	99.99	100.01	100.00	100.00
V						20	19	29			96	104	101	107
Cr						<20	<20	<20			1	10	10	19
Co											34	30	30	32
Ni						<10	<10	<10			11	12	13	14
Cu											25	16	24	23
Zn						53	50	56	98	103	58	59	65	70
Ga											18	17	18	19
Ge											1	1	1	2
Rb	50	50	90	85	74	72	80	84	88	101	94.5	99.8	103.9	88.5
Sr	470	470	540	580	650	590	600	580	595	564	511.8	487	488.8	580.5
Y	22	22	25	27	24	26	26	16	29	28	25.4	26.2	24.6	25.1
Zr	138	138	160	170	166	170	176	160	173	156	163.9	152.8	168.4	170.9
Nb	11	11	10	13	14	14	14	10	17	14	13.9	14.1	14.3	13.8
Mo											1.8	1.9	2.1	2.1
Ba	720	720	900	900	850	850	930	910	915	962	935	1017	991	989
La	30	30	43	35	38	<30	<30	<30	44	42	40	31	43	45
Ce	50	50	78	76	74	66	62	64	82	76	59	63	69	78
Pr											11	12	9	12
Nd									47	34	26	43	32	34
Sm											6	5	6	7
Pb									38	55	16	17	18	15
Th									25	22	13	14	15	11
Cl											162	191	176	397

Major elements in wt%; trace elements in ppm. Source: L96 = Lipman et al. 1996; R91 = Riciputi 1991; TS = This Study

Fig. 2 Silica variation diagrams (data from Askren et al. 1991; Riciputi 1991; this study; Lipman et al. 1996) for the MPT and Sheep Mountain Andesite (SMA). The MPT sample at ~68% SiO_2 (Lipman et al. 1996) is from the upper part of the MPT and has likely accumulated ash leading to a higher silica content than other analyzed samples
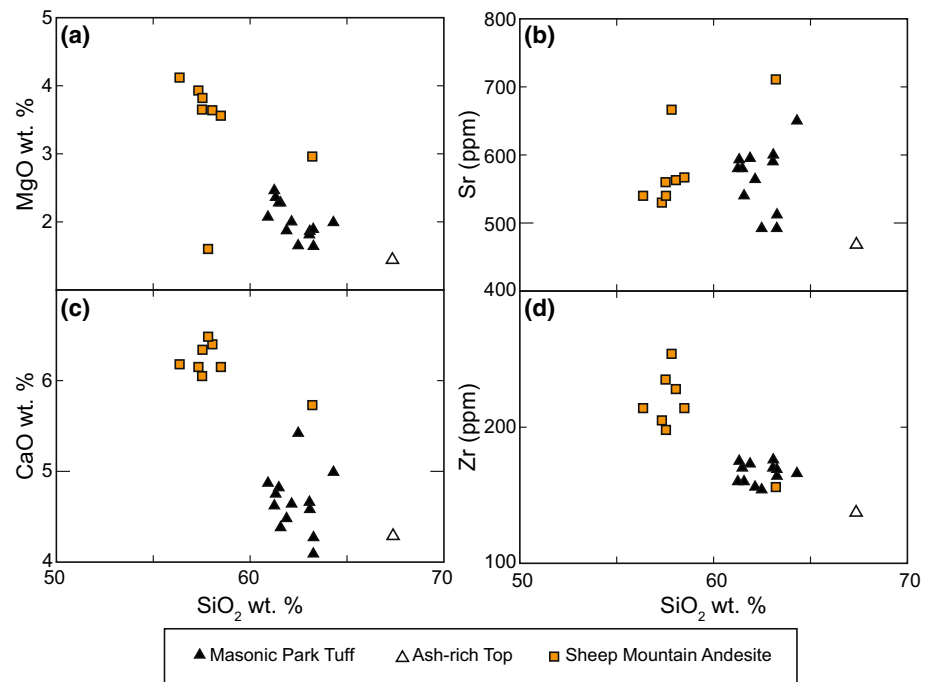
Sampling and analytical methods

Thirteen MPT samples were analyzed for whole-rock (4) or mineral chemistry (9). Whole-rock and petrographic data for ten additional samples from previous studies are also tabulated and plotted (Table 1, S1; Fig. 2). Samples were collected from a number of localities near South Fork, CO and Saddle Mountain (Fig. 1).

Major and trace-element data were obtained with a Philips PW2400 WD-XRF at UC Berkeley. Major elements were determined on 0.5 g of sample mixed with 3.5 g of lithium tetraborate flux that was fused into a glass disc. Trace-element concentrations were determined by pressing 3 g of homogenized sample powder into a pill for XRF analysis. Electron probe microanalysis (EPMA) analyses were done at the University of Washington with a 733 SuperProbe using an accelerating voltage of 15 kV and beam currents and spot sizes appropriate for each phase (Supplementary Appendix). Traverses in pyroxenes were measured at ETHZ using a Jeol 8200 EPMA at similar conditions also using wavelength dispersive X-ray spectroscopy. Backscattered electron (BSE) images were taken on the EPMA at the University of Washington as well as with a scanning electron microscope (Jeol 6390 LA) at ETHZ.

Trace-element concentrations in plagioclase crystals were measured by laser ablation ICP-MS at the Washington State University Geoanalytical Lab. Samples were analyzed on a Finnigan Element 2 HR-ICP-MS with a New Wave UP-213 laser using a ~120 μm raster and 10 micron spot size for 60 s on the following elements: Mg, Si, Ca, Ti, Rb, Sr, Y, Cs, Ba, La, Ce, Pr, Nd, Sm, Eu, Gd, Tb, and Pb

(Fe was measured by EPMA). NIST 612 glass and Si-29 were used as external and internal standards, respectively. The variability of SiO_2 in each zone was accounted for in the error of the internal standard by treating the EPMA SiO_2 analyses across the raster area as a population. When variability in SiO_2 was less than the error of the aforementioned analyses, the SiO_2 value with the largest error in a raster zone was used to maximize error. Measurements were taken in microlites as well as inboard and outboard of the anorthite spikes near the rims of plagioclase crystals. Values were recalculated using the Pepita algorithm (Dunkl et al. 2008).

Phase maps for MPT and FCT samples were obtained using the SEM-EDS systems at ETHZ and Colorado School of Mines. At ETHZ, the phase maps were generated from thin sections using spectral imaging (SI) data sets recorded on a Thermo Fisher Solid State Detector (SSD) EDS system (running NORAN NSS7 software) attached to a Jeol JSM-6390 LA scanning electron microscope operating at 15 kV acceleration voltage and a beam current of 7.5 nA. The phase maps are assembled from up to 40 individually measured spectral images; each with a dimension of 256×192 pixels and a spatial resolution of 10 μm/pixel. Pixel-to-phase assignments were carried out using the open source package *iSpectra* written for the data analysis software Igor Pro (Liebske 2015).

At the Colorado School of Mines, the QEMSCAN analyses were also conducted on carbon-coated thin sections using a Zeiss EVO 50 scanning electron microscope (SEM) equipped with four Bruker X275HR silicon drift X-ray detectors. All data are processed using the

iMeasure-iDiscover® software suite produced by FEI Inc. Instrument calibration (beam alignment, beam focusing, and beam current optimization, backscatter electron range calibration, and X-ray detector calibration) was performed prior to each analysis. Full thin section scans were conducted on all samples using a 25 μm beam step size. All analyses were conducted in Field Image mode. Four energy dispersive X-ray (EDS) spectrometers acquired spectra from each point along the beam stepping interval with an acceleration voltage of 25 kV, a beam current of 5 nA, and a beam size of roughly 1 μm. 1000 total X-ray counts were acquired for each spectrum. The EDS spectra and backscatter electron signal intensity were compared to mineral and amorphous phase definitions within a species identification protocol (SIP) list. Based on this first fit comparison, each acquisition point was assigned a composition from the SIP list. This assignment does not distinguish between amorphous phases, mineral interfaces, and different polymorphs with the same composition. Verification of correct species assignment was confirmed by transmitted and reflected light microscopy. The SIP list was reduced by grouping appropriate definitions together for each scan, and colors were assigned to each group in order to produce the false-color mineral maps.

Zircon crystals were separated, chemically abraded (Mattinson 2005), mounted using the standard laboratory procedures, and imaged by cathodoluminescence (CL) to help in avoiding xenocrystic cores during analysis. CL images were obtained using an FEI Quanta 200 FEG equipped with a GATAN MiniCL detector at the Scientific Center for Optical and Electron Microscopy (ScopeM) at ETHZ. U–Pb ages and trace-element analyses were done via laser ablation-inductively-coupled-plasma mass spectrometry (LA-ICP-MS) at ETH using an ASI Resolution 155 model 193 nm ArF excimer laser connected to a Thermo Element XR sector field ICP-MS. Spot analyses measured 30 μm at 5 Hz and ~2.5 J cm^{-2} and consisted of three cleaning pulses followed by 17 s washout, 29 s background measurement and 40 s ablation time. Analyses were standardized using the GJ-1 standard reference zircon (Jackson et al. 2004) with a reference age of 601.9 Ma (Horstwood et al. 2016) for U–Pb age determinations. Secondary reference zircon Temora2 (Black et al. 2004) was used for quality control. NIST-610 was used for trace-element analyses, and to obtain the best possible ages and trace-element analyses, the two methods were run individually on separate days on the same zircons. Data reduction was carried out in Iolite v2.5 (Paton et al. 2011) using the VizualAge (Petrus and Kamber 2012) and Trace_Elements IS (Paton et al. 2011) data reduction schemes. Decay constants of Jaffey et al. (1971) were used for age determination, and ages were Th-corrected using the method of Schärer (1984) and a Th/U$_{magma}$ of 3.

Bulk-rock chemistry

The MPT, while relatively homogeneous at outcrop and thin section scales (at least modally), displays some variability in whole-rock composition (Fig. 2; Table 1; Lipman et al. 1996). Most chemical analyses are from bulk tuff samples; pumice fragments are typically too small to analyze as whole-rock samples. Whole-rock SiO_2 concentrations of bulk tuff samples range from 62 to 68 wt% (Fig. 2; Table 1; Lipman et al. 1996), but cluster between 63 and 65 wt% SiO_2. Some of the observed chemical variations are due to eruption and emplacement processes, such as crystal-ash fractionation during transport (e.g., "ash elutriation"; Lipman 1967; Walker 1972). For example, the analyzed sample with the highest silica (Fig. 2; ~68 wt% SiO_2) is from the ash-rich top of the MPT (Lipman et al. 1996), while other bulk samples (Fig. S6) have higher crystallinities (up to 55 vol%). For comparison, bulk rock analyses of SMA lavas (likely derived from multiple vents), overlying the MPT, are also plotted in Fig. 2. Note that variability in elemental concentrations within these two units cannot be explained by simple mixing.

Crystal contents in pumices average 45% by volume (including vesicles), and range from 39 to 51% in the few bulk samples measured (Table 2; Fig. 3, S6–S7). The main phenocrysts are plagioclase, biotite, clinopyroxene, and Fe–Ti oxides with minor apatite and zircon. Quartz, while modally abundant (2–7%), is only present as devitrification microlites and does not form phenocrysts. Minor plagioclase microlites are also present in the devitrified shard matrix. The matrix is mostly too devitrified to analyze by EPMA; rare glassy samples suggest high-SiO_2 rhyolite with variable Ba contents (74–78 wt% SiO_2; 230–3800 ppm Ba; Table 3). Secondary alteration of this glass (as demonstrated by the presence of clay minerals in thin section; Fig. 3, S6–S7) is unlikely to have strongly affected the Ba content.

Mineral textures and phase chemistry composition

Plagioclase

Plagioclase is the most abundant mineral in the MPT (~26–40 modal %, present both as phenocrysts and

Table 2 Mineral proportions of representative MPT bulk ignimbrite samples in modal percent

Sample Number	Glass	Plagioclase	Biotite	Oxides	Pyroxene
86MD-187MP	54	40	5	1.3	0.5
86MD-203MP	49	37	9	2.3	2.3
MPT08-7	51	35	8.5	3	2.8
MPT08-1a	61	27	6.5	2.5	2.9

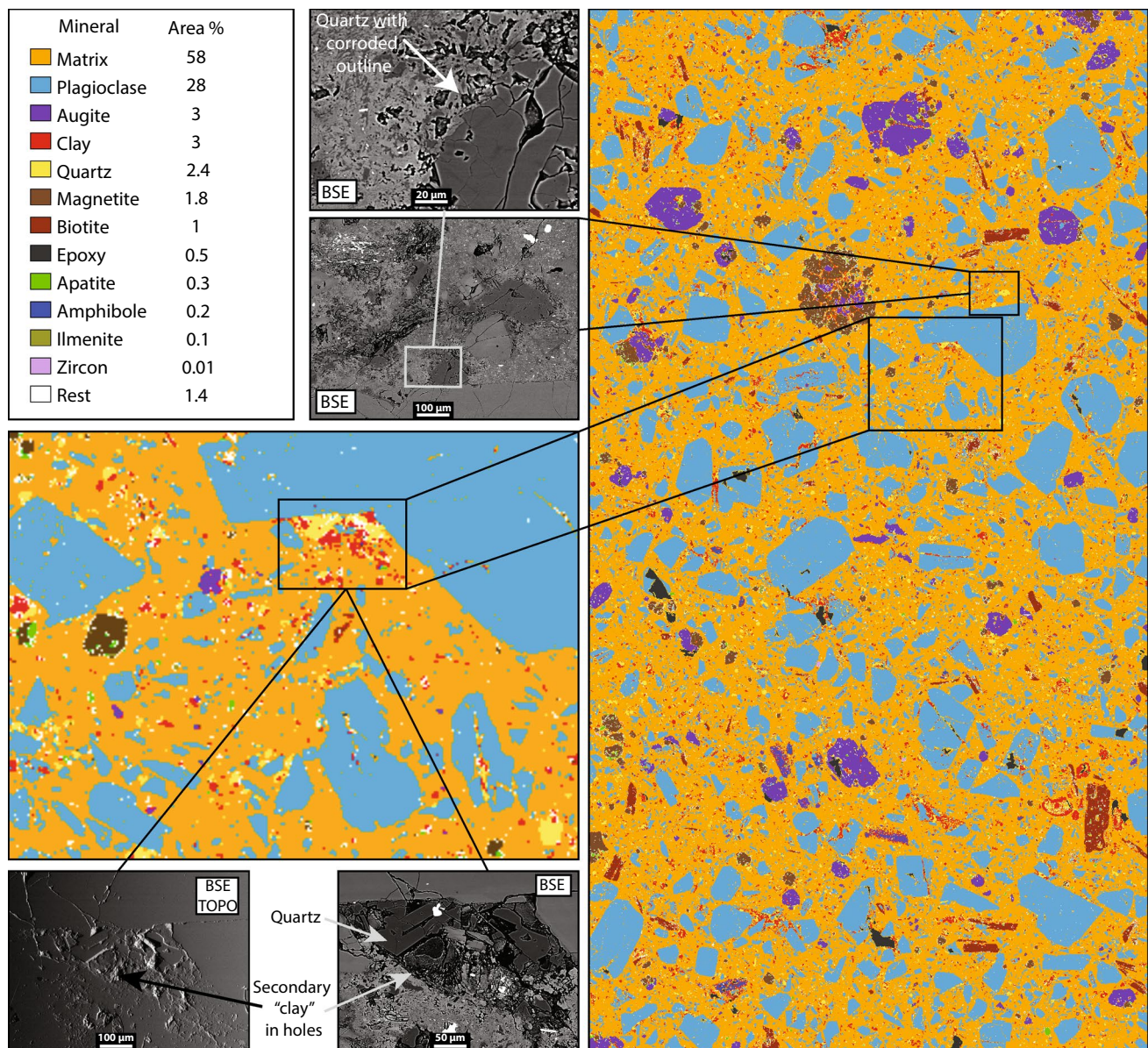| Mineral	Area %
Matrix	58
Plagioclase	28
Augite	3
Clay	3
Quartz	2.4
Magnetite	1.8
Biotite	1
Epoxy	0.5
Apatite	0.3
Amphibole	0.2
Ilmenite	0.1
Zircon	0.01
Rest	1.4

Fig. 3 Phase map for sample MPT08-1c and BSE images of quartz microlites with corroded rims. The BSE topo image indicates a depression presumably due to the weathering/alteration of volcanic glass to clay minerals

microlites; see Table 2, S2; Fig. 3, S6–S7). Phenocrysts are 0.3–4 mm in size; most are tabular to rectangular. Most crystals have low-An oscillatory-zoned interiors (average An_{36}) that are circumscribed by distinctive dissolution surfaces that are overgrown by An-rich rims (to An_{60}; Figs. 4, 5, 6, 7). These calcic zones revert outward to more normal values (~An_{40}). Such textures are similar to those in the 1991 deposits at Pinatubo (Fig. 6H of Pallister et al. 1996). The truncation surfaces and surrounding rims were an initial motivation for investigating the evolution of the MPT magma. Microlites tend to have An-contents that are similar to the high-An portions of post-resorption phenocryst

rims (An_{40-60}; Figs. 5, 6). A few phenocrysts have small, corroded, high-An cores (>An_{70}, not shown in figures).

Trace-element concentrations vary significantly between the low-An interiors vs high-An phenocryst rims and microlites (Fig. 6). As trace-element concentrations in plagioclase are strongly dependent on the An-content and temperature of crystallization, we recalculated trace-element contents in the silicate melt in equilibrium with the analyzed plagioclase compositions (inboard of high-An rims) using the method of Bindeman et al. (1998), assuming a temperature of 750 °C (see thermobarometric results below). Calculated Ba and Sr concentrations in the melt

Table 3 Representative glass analyses

Label	G12	G1.1	G1	G3
Sample	MPT08-4	MPT08-1a	MPT09-03	MPT08-5
SiO_2	76.38	74.52	77.50	77.20
TiO_2	0.20	0.25	0.18	0.19
Al_2O_3	12.44	13.79	12.79	12.07
FeO	0.34	0.42	0.53	0.54
MgO	0.00	0.02	0.15	0.05
CaO	0.13	0.68	0.83	0.29
BaO	0.43	0.12	0.12	0.03
SrO	0.00	0.10	0.00	0.00
Na_2O	2.08	3.18	3.44	2.27
K_2O	8.00	6.91	4.47	7.36
Total	100.00	100.00	100.00	100.00
Ba	3829	1084	1003	232

All analyses normalized to 100% anhydrous

Ba in ppm; all other elements in wt%

range, respectively, from ~300 to ~1600 ppm and ~100 to 360 ppm from low- to high-An regions of plagioclase crystals (Fig. 7). Increasing the temperature to 850 °C for the high-An plagioclase does not change the general trend, but it does increase calculated trace-element concentrations in the melt. For example, in An_{60} plagioclase, a temperature change of 100 °C, from 750 to 850 °C, leads to an increase in Sr of 37 ppm as well as a decrease in Ba of 277 ppm in the equilibrated melt. Both Ti and Rb contents are also elevated in high-An rims and microlites (Rb up to 300–400 ppm, Ti reaches >8000 ppm in calculated melt composition; Fig. 7).

Biotite

Biotite (1–9 modal %, Table 2, S3; Figs. 3, 8, S6–S7) is the most abundant ferromagnesian phase in MPT. Crystals are mostly tabular to rectangular, 0.5 to 4 mm in size. Inclusions of Fe-Ti oxides and apatite are common. Most crystals are only weakly zoned, the Mg# varying from 0.40 to 0.46 (Mg # calculated as $Mg^{2+}/(Mg^{2+} + Fe^{2+})$) and K_2O from 8.5 to 10.1 wt%. Fluorine concentration increases from <0.5 in mineral cores to ~2 wt% in the outer 50–100 microns of many crystal rims (Fig. 8; Table S3). These near-rim F-gradients do not correlate with variations in Fe and Mg.

Clinopyroxene

Clinopyroxene phenocrysts are present in all samples (<2–3 modal %, Table 2, S4; Fig. 3, S6–S7). Crystals range in size from 0.2 to >1 mm. Many grains appear euhedral, although some corrosion features are visible at the rims of crystals (Fig. 9). Complex, albeit limited, oscillatory zoning patterns are typical; Fe, Mg, and Al concentrations vary throughout crystals, and many display small, but analytically robust, increases in MgO contents near rims (Fig. 9). Clinopyroxene crystals commonly contain inclusions of

Fig. 4 Representative plagioclase textures and zoning patterns as both **a, b** Normarski and **c, d** backscatter electron images with EPMA traverses (*arrows* indicate the direction and length of traverse). Resorption textures (indicated by *black arrows*) are common near euhedral overgrowth rims; some larger crystals display multiple resorption surfaces
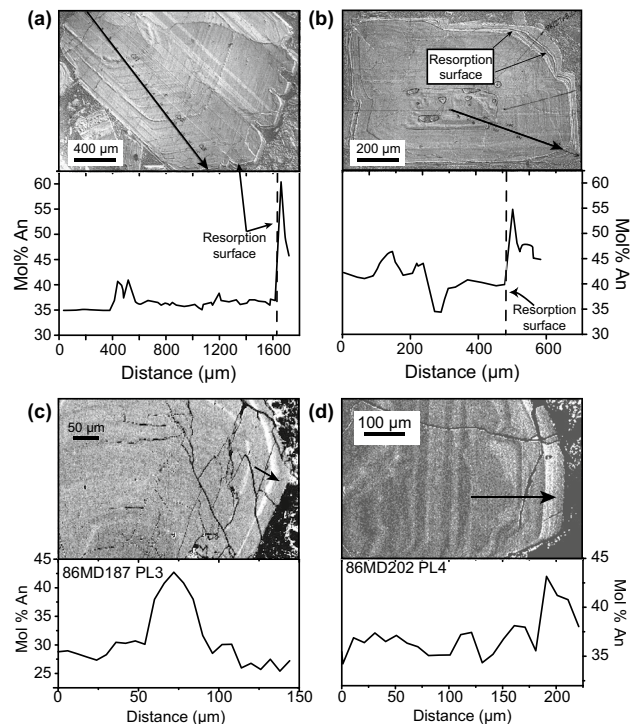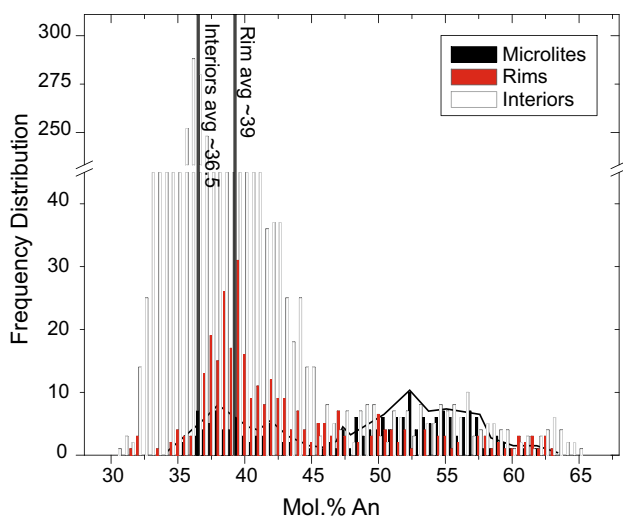
Fig. 5 Histogram of the An-content of plagioclase (interiors, rims, and microlites). The average An-content of the rims is higher than the interiors

apatite, Fe–Ti oxides, and rare biotite. Compositions of clinopyroxene in the lavas of Sheep Mountain Andesite, which overlies the MPT, are significantly more Fe rich and Ca poor (Fig. 10).

Quartz

Quartz forms only microlites in the studied samples (Fig. 3, S6–S7); matrix melt zones that are rich in SiO_2 also surround mafic minerals and glomerocrysts. Such small corroded quartz phenocrysts and SiO_2-rich zones sum to at most ~1–2% of thin section area. Additional fine-grain quartz (up to several % of area) is scattered in the matrix and is likely produced by devitrification or vapor-phase crystallization.

Zircon

Abundant zircons in heavy mineral separates display typical oscillatory (occasionally sector) zoning in CL. A minority of zircons have xenocrystic cores that were not analyzed. U varies between ~100–1000 ppm (~300 ppm average); Th/U ratios are ~0.4 (Table S5). Total REE content is ~2000–5000 ppm, while Ti concentrations vary between 2 and 15 ppm. Crystallization temperatures of 650–800 °C were determined using the calibration of Ferry and Watson (2007). Yb/Dy is typically in the range of 2–11 and varies inversely with temperature (Fig. 11). Newly determined LA-ICP-MS U-Pb ages range from ~27.5–31.9 Ma (Fig. 12, Table S5) with a weighted mean
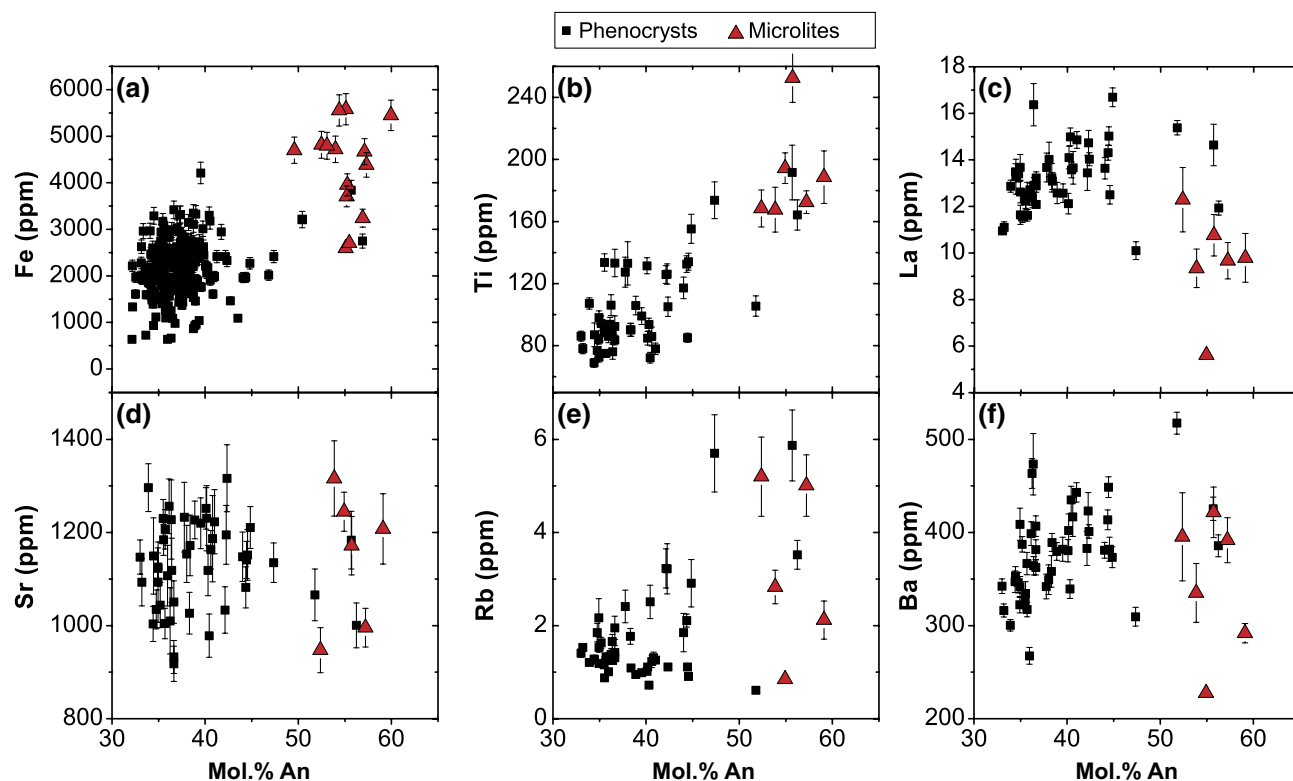
Fig. 6 Concentrations of trace elements in plagioclase phenocrysts and microlites. Fe was determined by EPMA; other elements by LA-ICP-MS. Indicated uncertainties are 1σ

Fig. 7 MPT trace-element concentrations for coexisting melts calculated using An-sensitive plagioclase-melt partition coefficients (Bindeman et al. 1998). *Open symbols* were calculated with variable temperatures (e.g., higher temperatures for higher An-content plagioclase); *closed symbols* were calculated with a fixed temperature (750 °C). High Sr and Ba concentrations in An-rich crystals suggest that feldspar may have been resorbed during the evolution of the MPT melt compositions
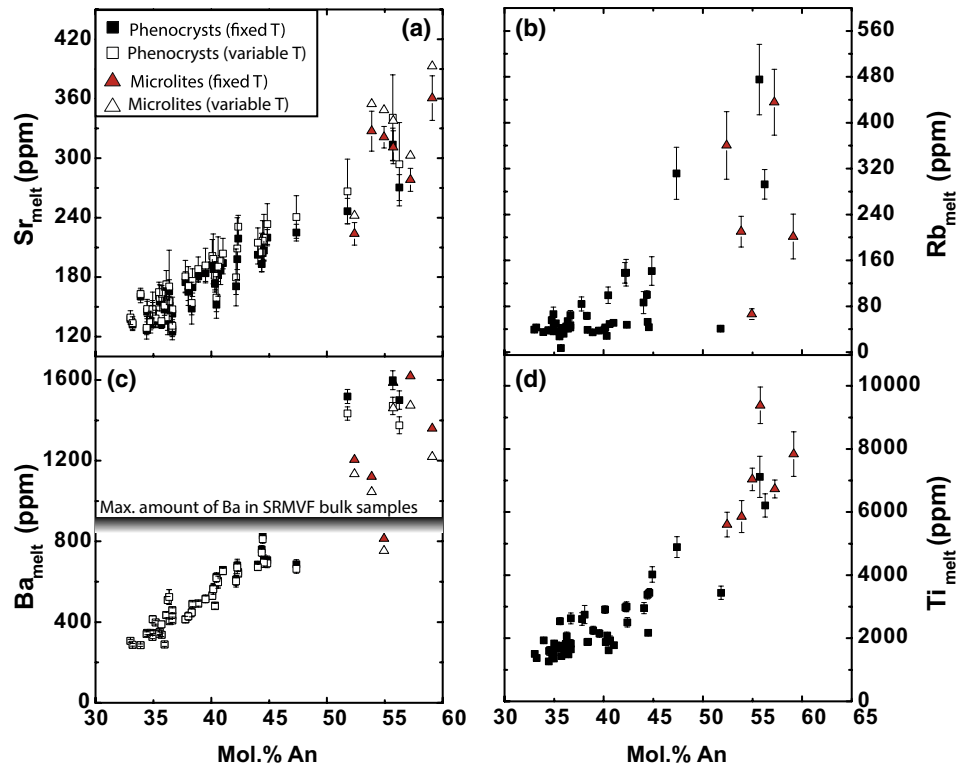
Fig. 8 EPMA traverses of two representative biotite crystals. The only significant zoning is increased F towards the rims
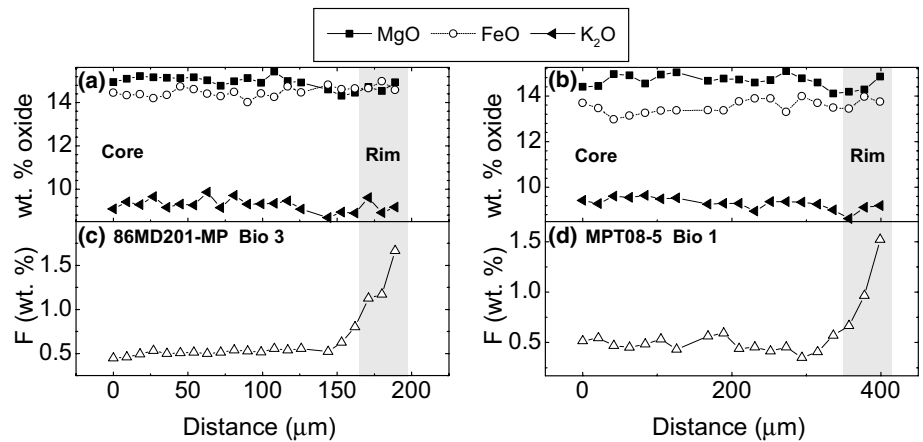
of 29.05 ± 0.30 Ma and a typical 2σ of ~0.8 Ma (2.7%). A mean square weighted deviates (MSWD) value of 4.4 suggests that either errors were underestimated or the data are over-dispersed (non-Gaussian). Because the MSWDs for the AusZ7-1 and 91,500 zircon standards were 0.9 ($n = 34$) and 1.5 ($n = 32$), respectively, we propose that error propagation was accurate and that the data record a prolonged crystallization duration. One analysis fall below the $^{40}Ar/^{39}Ar$ ages of the Masonic Park, indicating some bias in age determination that cannot be attributed to Pb loss in these chemically abraded zircons.

Accessory and alteration minerals

Other accessory phases include Fe–Ti oxides (ilmenite, magnetite) and apatite (Fig. 3, S6–S7) but, importantly, no titanite or amphibole. These phases are typically less than ~2% modal, but appear in the phase maps. Fe–Ti oxides are often resorbed and out of chemical equilibrium (see next paragraph). Apatite forms common inclusions in other phases, particularly biotite. Zones that are coated with clay material form small depressions in the thin sections, as indicated in topographic BSE images (Fig. S6); these likely resulted from weathering or vapor-phase crystallization.
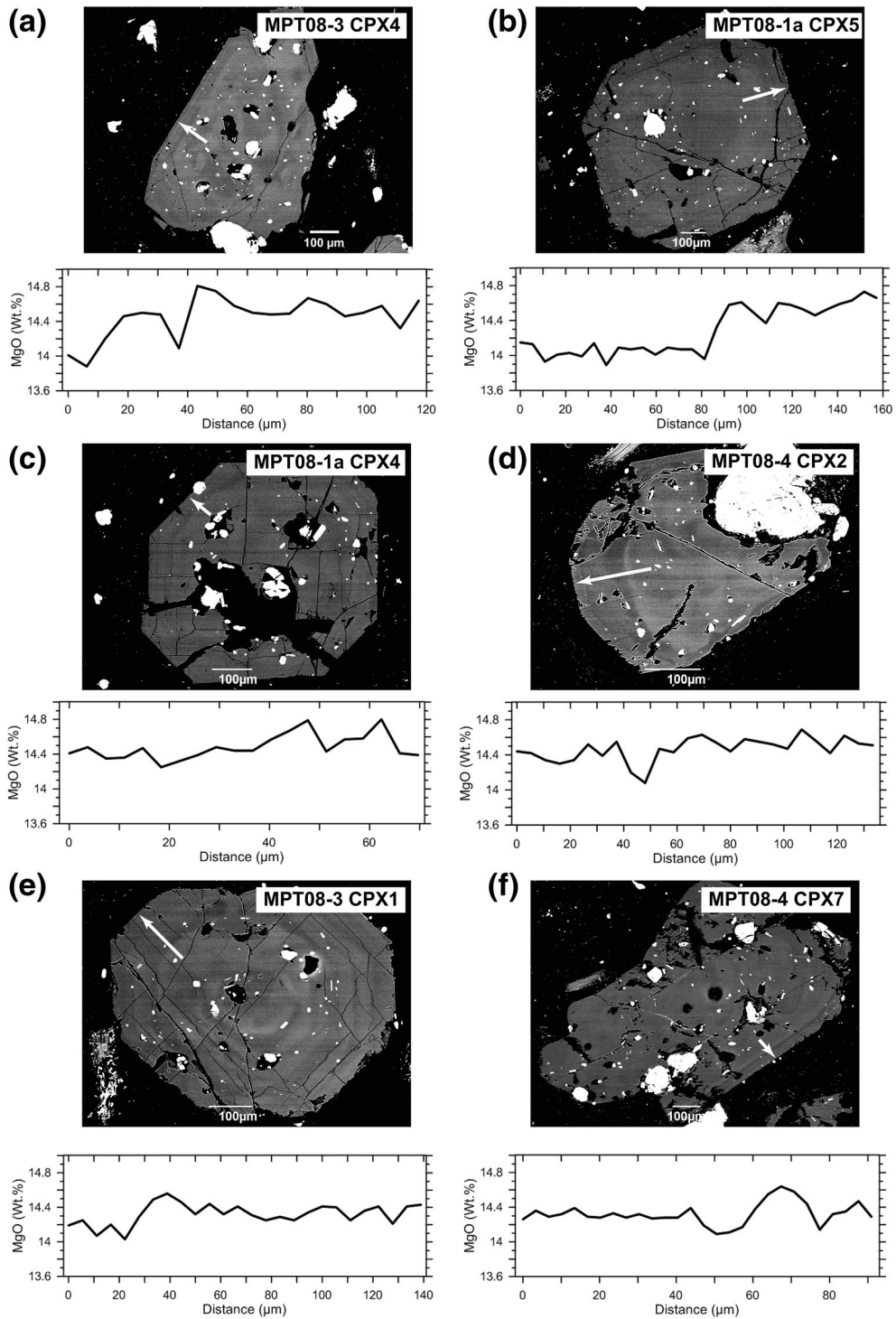
Fig. 9 a–e Examples of clinopyroxene textures (BSE images) and EPMA traverses (MgO wt% displayed) in the MPT. White regions in BSE images are others phases (mostly inclusions of Fe–Ti oxides, apatite, or plagioclase). Distance in traverses increases in the direction of the arrowheads in BSE images. Note that there is a tendency for MgO content to increase toward the rims
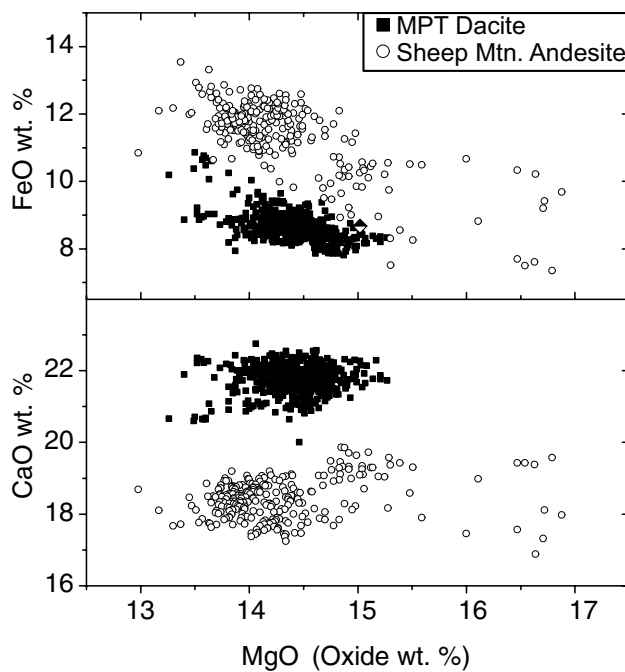
Fig. 10 Comparison of MgO, FeO, and CaO concentrations of clinopyroxene from MPT and post-MPT andesitic lavas (Sheep Mountain Andesite). Clinopyroxenes from MPT are distinct from those in the andesites
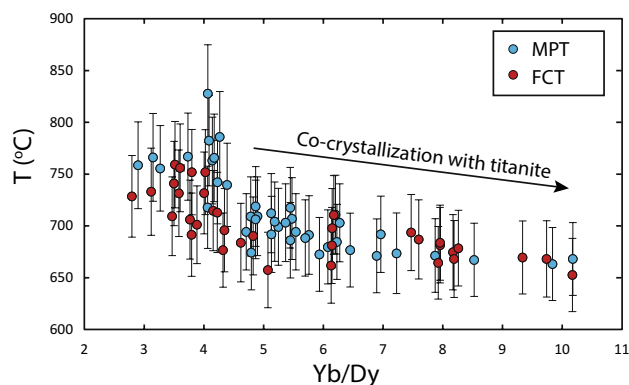
Fig. 11 Comparison of Fish Canyon Tuff (FCT) and Masonic Park Tuff (MPT) Yb/Dy ratios and temperature determinations, based pm the model of (Ferry and Watson 2007). The trend of increasing Yb/Dy was previously interpreted as a titanite fractionation in the FCT (Wotzlaw et al. 2013). The two trends are similar despite the absence of titanite in the MPT, which suggests that titanite was co-crystallizing with zircon in the MPT

Discussion

Pre-eruptive magma chamber conditions

Pre-eruptive magma chamber conditions are difficult to constrain for MPT. Ilmenite and magnetite are strongly exsolved and largely in Mg–Mn disequilibrium, likely due
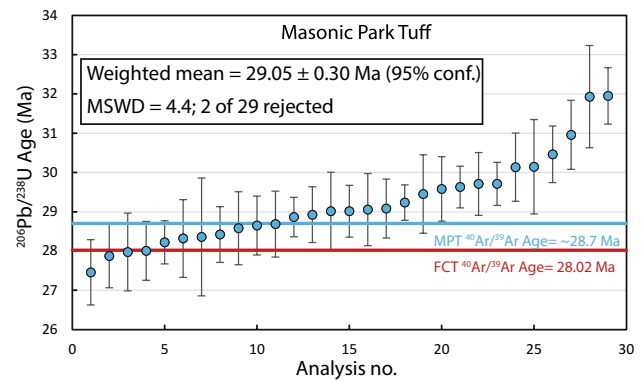
Fig. 12 $^{206}Pb/^{238}U$ zircon age for the Masonic Park tuff by LA-ICP-MS, rank ordered. Zircon ages yield a weighted mean of 29.09 ± 0.30 Ma (95% confidence) with an MSWD of 4.4, indicating some residence time. Comparison with FCT and MPT $^{40}Ar/^{39}Ar$ ages demonstrates that some systematic bias persists in these age determinations, even after chemical abrasion. Pb loss can be ruled out because of chemical abrasion, and the bias is likely due to matrix effects during laser ablation

to slow cooling in thick welded ash-flow deposits (Lipman et al. 1996). A few Fe–Ti oxide pairs, even though in apparent Mg-Mn equilibrium, yield calculated temperatures below the solidus (~300 °C; Ghiorso and Evans 2008). Thermometry and barometry for clinopyroxene-melt pairs were calculated according to the methods of Putirka (2008), assuming a values of ~4 wt% H_2O (a reasonable value for an arc dacite containing biotite and pyroxene but little to no hornblende; Costa et al. 2004) and the bulk-rock composition from sample MPT08-2AE. Equilibrium conditions were obtained at a Fe^{2+}/Fe^{3+} ratio of 0.65, indicating that the melt was fairly oxidized. Temperature estimates (eq. 34 of Putirka 2008) indicate that pyroxenes would crystallize from the hydrous melt at ~970–980 °C, consistent with our MELTS model (Fig. S8), where pyroxene is the near-liquidus phase. Pressures estimated using any version of eq. 32 from Putirka (2008) resulted in variable values (above 10 kb for eq. 32a, between −0.5 to nearly 4 kb for eq. 32b, and all negative for eq. 32c). Hence, we consider these pressure estimates unreliable for the Masonic Park Tuff.

The lack of sanidine and quartz in the MPT implies temperatures above ~825 °C for water-rich magma at upper crustal conditions, based on experimental work (Johnson and Rutherford 1989; Costa et al. 2004). Using PhasePlot 2.0 (Gualda et al. 2012) for the MPT bulk rock composition (MPT08-2EA) at NNO and 4 wt% H_2O, phase equilibria computed by Rhyolite-MELTS agree well with the natural mineral assemblage at ~170 MPa and slightly lower temperature (~780 °C). Rhyolite-MELTS at these conditions (dacitic initial composition, upper crustal pressure, 4 wt% H_2O) yields nearly fully crystalline magma with more than

20 modal % of both sanidine and quartz at ~740 °C (Fig. S8).

Although titanite is absent from the MPT mineral assemblage, Yb/Dy ratios and temperature relations indicate that it co-crystallized with zircon. Calculated zircon crystallization temperatures, using the method of Ferry and Watson (2007), assuming a_{SiO2} at unity and $a_{TiO2} = 0.7 \pm 0.1$ (1σ) to account for probable variations in titania activity (Ghiorso and Gualda 2013), suggest a range (~650–800 °C). These correlate negatively with Yb/Dy ratios, albeit with large errors corresponding to uncertainties in a_{TiO2} (Fig. 11). Wotzlaw et al. (2013) demonstrated that increasing Yb/Dy in the FCT results from titanite crystallization at lower temperatures. The low-temperature MPT zircons, with high Yb/Dy ratios comparable to the FCT, suggest that titanite co-crystallized with zircon, and its absence in the current mineral assemblage requires that it, as well as quartz and sanidine, was resorbed during reactivation of the magma (discussed in the following).

The origin of textural and geochemical heterogeneities in the MPT mush

Petrographic and chemical evidence indicate that the mineral-melt disequilibrium in MPT is related to reheating of the crystal mush shortly before eruption. Evidence includes: (1) widespread and pronounced dissolution surfaces near the edges of plagioclase crystals, followed by the growth of high-An rims and microlites; (2) reverse zoning (increased MgO near rims) in clinopyroxene phenocrysts; (3) dissolution of sanidine, as inferred by trace-element data in plagioclase rims and microlites; (4) dissolution of quartz, as shown by Si-rich zones and small, resorbed microlites; (5) dissolution of titanite, inferred from the titanite-fractionating signature preserved in zircon and the absence of titanite in the mineral assemblage; and (6) increased F independent of the Fe/Mg ratio at the rims of biotite, suggesting a rise in temperature and/or HF in the melt (Munoz 1984) or alternatively, vapor-phase alteration.

Reheating of the MPT magma body may have occurred shortly before eruption, as the high-An and high-MgO rims that grew on plagioclase and clinopyroxene phenocrysts, respectively, are only a few microns thick (assuming no time lag between dissolution and recrystallization in the case of plagioclase). The presence of andesites stratigraphically above and below MPT (Sheep Mountain Andesite, Conejos Formation) suggests that andesitic recharge likely carried the heat for the late-stage thermal perturbation of the upper crustal MPT reservoir.

Potential end-member mechanisms for such a reheating event are: (1) physical bulk mixing and mingling of a hotter, more mafic magma (probably andesite) with the upper crustal silicic magma (highly crystalline rhyodacite or

rhyolite mush), or (2) thermally-activated self-mixing of an upper crustal dacitic mush following magmatic underplating (Bachmann and Bergantz 2003; Burgisser and Bergantz 2011; Huber et al. 2011). This second end-member requires little or no physical mixing between the two magma bodies, apart from an influx of heat, minor melt, and volatiles from the underlying intrusion. Recharge from a near-liquidus (hence hotter) dacitic magma that ascended rapidly from the lower crust could also be envisaged (e.g., Crabtree and Lange 2011), but would be difficult to distinguish from self-mixing.

A comparison of the MPT whole-rock and mineral data to those of the post-MPT Sheep Mountain Andesite (SMA) suggests that bulk mixing with significant mass addition from a more mafic end-member (option 1) is unlikely. The reasons are as follows:

1. Most whole-rock major and trace elements do not approximate any mixing trends that would result from such a process (Fig. 2), even when accounting for some ash elutriation during MPT transport.
2. If silicic and mafic end-members had mixed, more clinopyroxene and plagioclase would be inherited from the mafic magma: for example, clearly mixed systems, such as Mt. Unzen (Browne et al. 2006), Montserrat (Murphy et al. 2000), or Volcán Quizapu (Ruprecht and Bachmann 2010; Ruprecht et al. 2012). However, clinopyroxene from MPT is chemically distinct from that in andesites from the same area (Fig. 10), and little high-An plagioclase could have been derived from andesitic sources (Fig. 6). High-An (>An_{50}) plagioclase occurs only as rare resorbed cores of large phenocrysts (mostly An_{35-40}) and in some microlites.
3. Trace-element concentrations in plagioclase do not record simple mixing with a more mafic melt. Although high-An plagioclase rims and microlites contain higher concentrations of some compatible elements (e.g., Sr and Ti), they also have high concentrations of elements that typically are incompatible (e.g., Rb and Ba; Fig. 6) and would not increase following mixing with a more mafic magma. For example, typical SRMVF andesites and dacites average ≤900 ppm Ba, but the high-An plagioclase crystallized from a melt with calculated Ba contents up to 1200–1600 ppm (Fig. 7). Hence, no plausible mixing end-member can explain the trace-element concentrations in the high-An plagioclase microlites and phenocryst rims.

Therefore, we interpret the compositions of MPT phenocrysts as recording significant reheating, melting of low-temperature sanidine, and late self-mixing, accompanied by limited mass addition from the underplated magma. The observed variations of Ba and Sr concentrations as a

function of An-content in plagioclase require co-crystallization of sanidine and plagioclase followed by partial remelting of these two phases during reheating. The low Ba concentrations in the evolved (low-An) MPT plagioclase phenocrysts (which translates into <300 ppm Ba in the melt using partition coefficients from Bindeman et al. (1998); Fig. 7) can be attained only if subsequently melted plagioclase and sanidine were co-crystallizing as the magma reached its highest crystallinity. This can be shown by quantitatively tracing the Ba evolution in the melt during fractional crystallization using phase proportions that can be estimated either: (1) with MELTS (Ghiorso and Sack 1995), which tends to overestimate clinopyroxene over biotite, or (2) with the clinopyroxene-biotite ratio fixed to that observed in MPT (Fig. 13). In the absence of sanidine (but including biotite), Ba melt concentrations remain high, inconsistent with the low Ba content of evolved plagioclase compositions. Ba decreases rapidly in silicic melt during sanidine crystallization, leading to Ba concentrations of
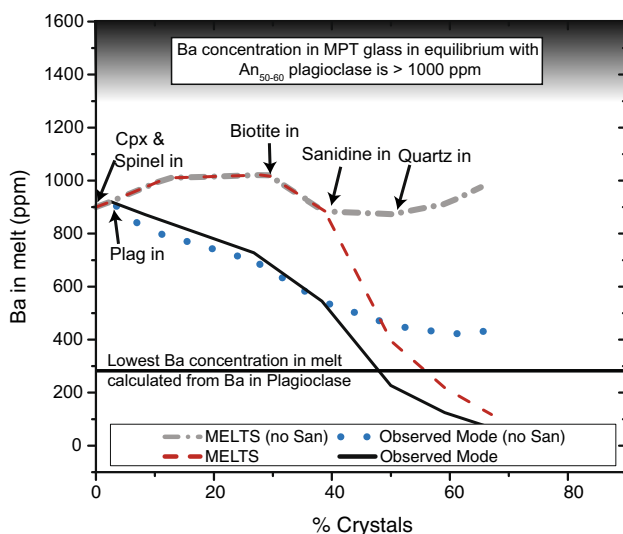
Fig. 13 Model of Ba evolution in the MPT as a function of crystallization. Partition coefficients are in Appendix A3. Barium is sensitive to the crystallization of both sanidine and biotite. An average sanidine partition coefficient (12) and a high biotite partition coefficient (8.7) were used to minimize estimates of sanidine resorption; a lower biotite coefficient would imply greater sanidine participation in controlling the concentration of Ba in the melt. Due to pervasive mineral zoning, an equilibrium-step model was used to calculate in which material from the previous steps cannot react with the material crystallized in a future step. Model runs with phase proportions calculated using the thermodynamic software MELTS-Rhyolite (Gualda et al. 2012). Average whole-rock compositions are marked "MELTS," (e.g., MELTS no San), while those with the proportion of biotite and clinopyroxene adjusted to match ratios in MPT samples are marked "Observed Mode". Models were run with and without sanidine stable. The line at 285 ppm Ba denotes the concentration of Ba in the melt in equilibrium with the lowest Ba contents measured in MPT plagioclase phenocrysts (Fig. 7)

<300 ppm after only 5.4–9% sanidine crystallization (total crystallinity ~50–58 vol%; Fig. 13). Conversely, the high Ba and Sr concentrations in microlites and phenocryst rims (higher than any plausible magmatic liquids in the area) are best explained by melting of sanidine (±biotite)+low-An plagioclase, followed by the crystallization of high-An plagioclase from a melt enriched in these two elements.

The higher concentrations of Fe and Ti-in plagioclase microlites and phenocryst rims indicate that either (1) Fe–Ti oxides partly dissolved during the reheating, as evidenced by their dominantly resorbed outlines and/or (2) some mass addition from a less-evolved melt+bubble mixture played a role. Given that no added crystalline mass was detected (e.g., clinopyroxene compositions are dramatically different from those in the inferred recharge; see Fig. 10), we postulate that the first mechanism was sufficient to generate the observed Fe- and Ti-rich microlites. We therefore infer that elevated concentrations of these two elements in microlites and phenocryst rims are in part the result of an increase in temperature following recharge and plagioclase resorption (Bindeman et al. 1998; Sugawara 2001), while noting that Fe concentration in plagioclase is sensitive to oxygen fugacity (Sugawara 2001).

Kinetic effects during the rapid crystallization of plagioclase microlites and rims are unlikely to have been significant in generating the observed zoning profiles. A boundary layer enriched in incompatible elements and depleted in compatible trace elements may develop at the crystal-melt interface at high growth rates (e.g., Albarede and Bottinga 1972; Bouvet; De Maisonneuve et al. 2013; Zellmer et al. 2016). However, if disequilibrium growth were dominant, compatible elements, such as Sr, would be depleted in rapidly crystallizing feldspar compared to those that grew under equilibrium conditions, whereas Ba would be only slightly enriched, because the Ba partition coefficient is close to unity. As Sr and Ba concentrations are higher in microlites and phenocryst rims, we conclude that disequilibrium growth was not a major factor in the trace-element partitioning in MPT plagioclase.

In light of the observations above, the textural and compositional characteristics of MPT are most likely the result of a rejuvenation event, triggered by the injection of hotter magmas from below. These injections led to limited mass addition of less-evolved melt and self-mixing during partial resorption of the crystalline mush (e.g., Huber et al. 2011; Wolff et al. 2015). These processes were followed by the late crystallization of high-An plagioclase, and slightly more Mg-rich rims in pyroxenes.

Time scales and mechanics of reactivation

Constraining the timescale associated with the pre-eruptive reactivation of MPT magma body is fundamental to

determine how quickly large magmas can erupt following thermal perturbations (e.g., Druitt et al. 2012; Matthews et al. 2012). The evidence for melting of MPT crystals suggests that crystallinity reduction following a magma recharge played an important role in this reactivation, as suggested for other units (e.g., Murphy et al. 2000; Bachmann et al. 2002; Molloy et al. 2008; Bachmann 2010; Cooper and Kent 2014; Klemetti and Clynne 2014). It is difficult to quantify how much crystalline mass melted, but the calculated Ba concentrations in the liquid (Fig. 7) roughly constrain a reduction of crystal mass at $> \sim 5$ vol% during reactivation. This value is based on the ~ 1000 ppm increase of Ba in the melt, largely due to sanidine resorption, assuming a maximum $\sim 20,000$ ppm in sanidine (e.g., Bachmann et al. 2014). The ~ 5 vol% melting of the crystalline mass is a minimum, as 20,000 ppm Ba is likely an overestimate, and quartz, low-An plagioclase, Fe–Ti oxides were also resorbed. Such a reduction in crystal content is slightly less than and has been suggested for the thermal rejuvenation of the Fish Canyon magma body based on trace elements in titanite (Wotzlaw et al. 2013).

We utilize the petrological and geochemical constraints described above for the MPT to apply a quantitative thermo-mechanical model, as originally developed by Huber et al., (2011). The key ingredients to evaluate the reactivation scenario are:

1. A minimum of ~ 5 vol% of the crystalline mass in a 500 km^3 magma was subjected to a phase change (melting).
2. A lack of pervasive mixing between mafic recharge and host magmas.
3. Phenocryst phases (plagioclase, clinopyroxene, biotite) display zoning patterns with relatively sharp, up-temperature changes in composition near their rims.

Melting of phenocrysts is associated with a decreased in density (increase in volume), which in turn leads to mechanical work (pressure increases within the partially melted mush layer in contact with the recharge). Because the lowermost portion of the mush, in contact with the reactivation front, is barely rigid, the overpressure build-up can mechanically destabilize a relatively thin layer (meter scale) of mush. Small fragments of mush that are located immediately above the reactivated portion of the mush are likely to be assimilated during this process. Huber et al. (2011) argue that this thermo-mechanical reactivation is energetically more efficient and rapid than melting alone, but the timescale for reactivation is strongly controlled by the thickness of the mush that must be reactivated. For magma bodies with volumes similar to MPT (~ 500 km^3), timescales are projected to be a few hundreds to a few thousands of years (Huber et al. 2012), depending on the

size and frequency of recharge inputs during this process. This thermo-mechanical reactivation involves crystallinity reduction (final crystallinity around 40–45 vol%, a few percent below the mechanical locking point) and is, therefore, consistent with the minimum 5 vol% decrease in crystallinity estimated for MPT.

Diffusion speedometry is widely used to measure reactivation timescales (e.g., Zellmer et al. 1999; Costa and Chakraborty 2004; Charlier et al. 2007; Turner and Costa 2007; Martin et al. 2008; Druitt et al. 2012; Matthews et al. 2012; Chamberlain et al. 2014), but this method is problematic for MPT. As described above, plagioclase and pyroxene display significant chemical zoning, but most zoning profiles are complex sawtooth patterns that are not easily amenable to diffusion modeling. Both phases display relatively sharp interfaces between zones close to the rims, without discernable diffusion profiles. In addition, variable zoning morphologies suggest that crystals responded in diverse ways to reheating, while other factors, including the location of the crystals in the magma chamber at the onset of reactivation and the amount of recharge events experienced, impacted their final individual texture, making the interpretation of diffusional timescales challenging. Furthermore, even detailed studies on smaller systems such as Montserrat may yield reactivation timescales that vary across three orders of magnitude (Zellmer et al. 2003). We therefore conclude that the best time estimate for reactivation of the MPT mush is likely at least several hundreds of years, as estimated from thermo-mechanical models for comparably large magma volumes (Huber et al. 2011). The time required to reach homogenization (as observed at hand sample scale) by mixing will be at least two orders of magnitude shorter (years to tens of years; Huber et al. 2012). This short mixing time is consistent with numerical simulations of rapid gas-driven overturn in high-viscosity systems (Ruprecht et al. 2008).

Comparison with FCT

Eruption of the FCT followed MPT by $\sim 700,000$ years, and with a volume ten times greater, it completely buried the MPT source caldera. Although these two ignimbrites are both crystal-rich calc-alkaline dacites, they differ in mineral assemblages: the FCT contains conspicuous phenocrysts of quartz. Amphibole and titanite appear in thin section, but the assemblage lacks clinopyroxene, and is devoid of plagioclase microlites. The FCT is also slightly more SiO_2- and K_2O rich than the MPT (average composition of 68 wt% SiO_2, 4.1 wt% K_2O vs 62.7 wt% SiO_2, 3.5 wt% K_2O, respectively) and erupted at a lower temperature (~ 710–$760\,^\circ$C, Bachmann and Dungan 2002, vs 800–850 $^\circ$C for the MPT). However, similar Ti-in zircon temperatures and ample evidence for more vigorous rejuvenation in the case of the

MPT suggest that the two may have indeed evolved to a similar temperature (assuming similar a_{SiO2} and a_{TiO2}). The presence of multiple hydrous phases in FCT and its lower eruption temperature than the MPT suggest that FCT magma evolved under slightly more water-rich conditions, although precise estimates of water content differences are difficult to obtain. Application of the plagioclase-liquid hygrometer of Waters and Lange (2015) to plagioclase rims (assuming 800–850 °C) yields water concentrations of ~13% in the MPT, comparable to those obtained from the FCT using temperatures from plagioclase-sanidine pairs (Bachmann et al. 2002). Nonetheless, the observation of amphibole presence in the FCT vs clinopyroxene in the MPT seemingly suggests a difference in water activity. However, since we cannot rule out that amphibole may have resorbed in the MPT (along with sanidine, quartz and titanite), we cannot say with certainty how the two differed with respect to water activity.

Despite their different volumes, mineralogy, and possibly water contents, the upper crustal FCT and MPT magma bodies or mush zones both were reheated and mechanically reactivated prior to eruption as indicated by: (1) highly resorbed (FCT) sanidine and quartz or totally dissolved (MPT) sanidine, titanite, and quartz and (2) reverse zoning in phenocrysts, most obvious in plagioclase, sanidine, and amphibole for the FCT (Bachmann and Dungan 2002; Bachmann et al. 2002) and in plagioclase and pyroxene in the MPT (this study). The presence of scarce mafic enclaves in late-erupted FCT (and perhaps in MPT) indicate that the rejuvenation event was likely triggered by a mafic recharge event that brought heat, volatiles, and some melt (but no crystalline debris) to these upper crustal crystal mushes (Bachmann and Bergantz 2003, 2006). Alternatively, the recharge could have been more evolved magmas, in which case mass addition would be very difficult to rule out given the similarities in composition with the main body of magma.

The difference in plagioclase compositional profiles between the MPT and FCT (i.e., presence of ubiquitous sharp An-rich spikes at the rims of most plagioclase phenocrysts in MPT in comparison with the more gradual rimward An increase in the FCT plagioclase) suggests that the rejuvenation event was shorter and more intense for MPT. In comparison, FCT underwent a progressive increase in temperature over an extended period, estimated to be ~200,000 years based on zircon geochronology and zircon trace-element chemistry (Wotzlaw et al. 2013). A more sudden reawakening of MPT is consistent with its smaller size, allowing a typical lower-crustal recharge event to have more impact on temperature and crystallinity of the dacitic mush than for the gigantic FCT. It is also possible that the highest crystallinity reached by the MPT at the coldest point of its evolution was less than that of FCT (estimated at ~75 vol% crystals; Wotzlaw et al. 2013), making it energetically less costly to rejuvenate.

Conclusions

MPT deposits have textural and chemical characteristics of a magmatic system that was substantially out of thermal and chemical equilibrium at the time of eruption. Extensively resorbed plagioclase, absence of sanidine, titanite, and only sparse corroded quartz microlites, along with inverse zoning in phenocrysts (plagioclase and clinopyroxene), indicate that the magma reservoir was reheated and reactivated shortly before eruption. Major and trace-element variations among whole-rock samples and crystals do not support simple mixing with a more mafic recharge as a mechanism for delivering the necessary heat. While a reheating event is evident given the chemical variation in thermally sensitive MPT phases (An in plagioclase, increased MgO concentrations in pyroxene rims), any model must account for this thermal rejuvenation with little mass addition of more mafic magma (crystalline debris is not observed).

We propose a model similar to that developed for FCT (Bachmann et al. 2002). The interaction of the Masonic Park Tuff reservoir with recharge magma has the following characteristics: (1) thermal reactivation due to initial heating and limited melt + gas addition following the underplating of a hot recharge magma; (2) resorption of low-temperature phases (e.g., sanidine, quartz, titanite, and low-An plagioclase) causing the crystalline framework to disaggregate, thereby leading to density instabilities that drive convective self-mixing; and (3) stirring of the crystal-rich magma by convective currents, leading to the observed textural and compositional homogeneity at hand-sample (and larger) scale. The similar rejuvenation signatures in two ignimbrites with different mineralogies, volumes, and pre-eruptive temperatures that were erupted from the same crustal site indicates that such a remobilization process may be a common precursor to the evacuation of crystal-rich dacitic mushes residing in the upper crust, even among eruptive volumes that differ by an order of magnitude.

References

Albarede F, Bottinga Y (1972) Kinetic disequilibrium in trace element partitioning between phenocrysts and host lava. Geochim Cosmochim Acta 36(2):141–156. doi:10.1016/0016-7037(72)90003-8

Annen C (2009) From plutons to magma chambers: Thermal constraints on the accumulation of eruptible silicic magma in the upper crust. Earth Planet Sci Lett 284(3–4):409–416. doi:10.1016/j.epsl.2009.05.006

Askren RR, Whitney JA, Roden MF (1991) Petrology and geochemistry of the Huerto Andesite, San Juan volcanic field, Colorado. Contrib Mineral Petrol 107:373–386. doi:10.1007/BF00325105

Bachmann O (2010) The petrologic evolution and pre-eruptive conditions of the rhyolitic Kos Plateau Tuff (Aegean arc). Cent Eur J Geosci 2(3):270–305. doi:10.2478/V10085-010-0009-4

Bachmann O, Bergantz GW (2003) Rejuvenation of the Fish Canyon magma body: a window into the evolution of large-volume silicic magma systems. Geology 31(9):789–792. doi:10.1130/G19764.1

Bachmann O, Bergantz GW (2006) Gas percolation in upper-crustal silicic crystal mushes as a mechanism for upward heat advection and rejuvenation of near-solidus magma bodies. J Volcanol Geotherm Res 149(1–2):85–102. doi:10.1016/j.jvolgeores.2005.06.002

Bachmann O, Dungan MA (2002) Temperature-induced Al-zoning in hornblendes of the Fish Canyon magma, Colorado. Am Mineral 87:1062–1076. doi:10.2138/am-2002-8-903

Bachmann O, Huber C (2016) Silicic magma reservoirs in the Earth's crust. Am Mineral 101(11):2377–2404. doi:10.2138/am-2016-5675

Bachmann O, Dungan MA, Lipman PW (2002) The Fish Canyon magma body, San Juan volcanic field, Colorado: rejuvenation and eruption of an upper-crustal batholith. J Petrol 43(8):1469–1503. doi:10.1093/Petrology/43.8.1469

Bachmann O, Charlier BLA, Lowenstern JB (2007) Zircon crystallization and recycling in the magma chamber of the rhyolitic Kos Plateau Tuff (Aegean Arc). Geology 35(1):73–76. doi:10.1130/G23151A.1

Bachmann O, Deering CD, Lipman PW, Plummer C (2014) Building zoned ignimbrites by recycling silicic cumulates: insight from the 1000 km³ Carpenter Ridge Tuff, CO. Contrib Mineral Petrol. doi:10.1007/s00410-014-1025-3

Barboni M, Boehnke P, Schmitt AK, Harrison TM, Shane P, Bouvier A-S, Baumgartner L (2016) Warm storage for arc magmas. Proc Natl Acad Sci USA. doi:10.1073/pnas.1616129113

Bindeman IN, Davis AM, Drake MJ (1998) Ion microprobe study of plagioclase-basalt partition experiments at natural concentration levels of trace elements. Geochim Cosmochim Acta 62(7):1175–1193. doi:10.1016/S0016-7037(98)00047-7

Black LP, Kamo SL, Allen CM, Davis DW, Aleinikoff JN, Valley JW, Mundil R, Campbell IH, Korsch RJ, Williams IS (2004) Improved 206 Pb/238 U microprobe geochronology by the monitoring of a trace-element-related matrix effect; SHRIMP, ID–TIMS, ELA–ICP–MS and oxygen isotope documentation for a series of zircon standards. Chem Geol 205(1):115–140. doi:10.1016/j.chemgeo.2004.01.003

Brown SJA, Fletcher IR (1999) SHRIMP U–Pb dating of the preeruption growth history of zircons from the 340 ka Whakamaru Ignimbrite, New Zealand: Evidence for>250

k.y. magma residence times. Geology 27(11):1035–1038. doi:10.1130/0091-7613(1999)027<1035:SUP.>2.3.CO;2

Browne BL, Eichelberger JC, Patino LC, Vogel TA, Uto K, Hoshizumi H (2006) Magma mingling as indicated by texture and Sr/Ba ratios of plagioclase phenocrysts from Unzen volcano, SW Japan. J Volcanol Geotherm Res 154(1–2):103–116. doi:10.1016/j.jvolgeores.2005.09.022

Burgisser A, Bergantz GW (2011) A rapid mechanism to remobilize and homogenize highly crystalline magma bodies. Nature 471(7337):212–215. doi:10.1038/nature09799

Chamberlain KJ, Morgan DJ, Wilson CJN (2014) Timescales of mixing and mobilisation in the Bishop Tuff magma body: perspectives from diffusion chronometry. Contrib Mineral Petrol 168(1):1–24. doi:10.1007/s00410-014-1034-2

Charlier BLA, Wilson CJN, Lowenstern JB, Blake S, Van Calsteren PW, Davidson JP (2005) Magma Generation at a Large, Hyperactive Silicic Volcano (Taupo, New Zealand) Revealed by U–Th and U–Pb Systematics in Zircons. J Petrol 46(1):3–32. doi:10.1093/petrology/egh060

Charlier BLA, Bachmann O, Davidson JP, Dungan MA, Morgan D (2007) The upper crustal evolution of a large silicic magma body: evidence from crystal-scale Rb/Sr Isotopic Heterogeneities in the Fish Canyon Magmatic System, Colorado. J Petrol 48(10):1875–1894. doi:10.1093/petrology/egm043

Claiborne LL, Miller CF, Flanagan DM, Clynne MA, Wooden JL (2010) Zircon reveals protracted magma storage and recycling beneath Mount St. Helens. Geology 38(11):1011–1014. doi:10.1130/g31285.1

Colucci MT, Dungan MA, Ferguson KM, Lipman PW, Moorbath S (1991) Precaldera lavas of the Southeast San-Juan volcanic field—parent magmas and crustal interactions. J Geophys Res Solid Earth 96(B8):13413–13434. doi:10.1029/91JB00282

Cooper KM, Kent AJR (2014) Rapid remobilization of magmatic crystals kept in cold storage. Nature 506(7489):480–483. doi:10.1038/nature12991

Costa F, Chakraborty S (2004) Decadal time gaps between mafic intrusion and silicic eruption obtained from chemical zoning patterns in olivine. Earth Planet Sci Lett 227:517–530. doi:10.1016/j.epsl.2004.08.011

Costa F, Scaillet B, Pichavant M (2004) Petrological and experimental constraints on the pre-eruption conditions of Holocene dacite from Volcan San Pedro (36 degrees S, Chilean Andes) and the importance of sulphur in silicic subduction-related magmas. J Petrol 45(4):855–881. doi:10.1093/petrology/egg114

Crabtree SM, Lange RA (2011) Complex phenocryst textures and zoning patterns in andesites and dacites: evidence of degassing-induced rapid crystallization? J Petrol 52(1):3–38. doi:10.1093/petrology/egq067

Crowley JL, Schoene B, Bowring SA (2007) U–Pb dating of zircon in the Bishop Tuff at the millennial scale. Geology 35:1123–1126. doi:10.1130/G24017A.1

De Maisonneuve CB, Dungan MA, Bachmann O, Burgisser A (2013) Petrological insights into shifts in Eruptive Styles at Volcan Llaima (Chile). J Petrol 54(2):393–420. doi:10.1093/petrology/egs073

Druitt TH, Costa F, Deloule E, Dungan M, Scaillet B (2012) Decadal to monthly timescales of magma transfer and reservoir growth at a caldera volcano. Nature 482(7383):77–80. doi:10.1038/nature10706

Dunkl I, Mikes T, Simon K, von Eynatten H (2008) Laser ablation ICP-MS in the earth sciences: current practices and outstanding issues. In: Sylvester P (ed) Short Course, vol 40. Mineralogical Association of Canada, pp 334–340

Ferry J, Watson E (2007) New thermodynamic models and revised calibrations for the Ti-in-zircon and Zr-in-rutile

thermometers. Contrib Mineral Petrol 154(4):429–437. doi:10.1007/s00410-007-0201-0

Gelman SE, Gutierrez FJ, Bachmann O (2013) On the longevity of large upper crustal silicic magma reservoirs. Geology 41:759–762. doi:10.1130/G34241.1

Ghiorso MS, Evans BW (2008) Thermodynamics of rhombohedral oxide solid solutions and a revision of the Fe–Ti oxide geothermometer and oxygen-barometer. Am J Sci 308(9):957–1039. doi:10.2475/09.2008.01

Ghiorso MS, Gualda GA (2013) A method for estimating the activity of titania in magmatic liquids from the compositions of coexisting rhombohedral and cubic iron–titanium oxides. Contrib Mineral Petrol 165(1):73–81. doi:10.1007/s00410-012-0792-y

Ghiorso MS, Sack RO (1995) Chemical mass transfer in magmatic processes IV: a revised and internally consistent thermodynamic model for the interpolation and extrapolation of liquid-solid equilibria in magmatic systems at elevated temperatures and pressures. Contrib Mineral Petrol 119:197–212. doi:10.1007/BF00307281

Gottsmann J, Lavallee Y, Marti J, Aguirre-Diaz G (2009) Magma-tectonic interaction and the eruption of silicic batholiths. Earth Planet Sci Lett 284(3–4):426–434. doi:10.1016/j.epsl.2009.05.008

Gualda GAR, Ghiorso MS, Lemons RV, Carley TL (2012) Rhyolite-MELTS: a modified calibration of MELTS optimized for silica-rich, fluid-bearing magmatic systems. J Petrol 53(5):875–890. doi:10.1093/petrology/egr080

Gutierrez FJ, Bachmann O, Parada MA, Payacán I, Gelman SE (2013) Late-stage magma flow in a shallow felsic reservoir: merging the anisotropy of magnetic susceptibility record with numerical simulations in La Gloria Pluton, central Chile. J Geophys Res 118:1–15. doi:10.1002/jgrb.50164

Hildreth W (1981) Gradients in silicic magma chambers: Implications for lithospheric magmatism. J Geophys Res 86(B11):10153–10192. doi:10.1029/JB086iB11p10153

Horstwood MS, Košler J, Gehrels G, Jackson SE, McLean NM, Paton C, Pearson NJ, Sircombe K, Sylvester P, Vermeesch P (2016) Community-derived standards for LA-ICP-MS U-(Th-) Pb geochronology–uncertainty propagation, age interpretation and data reporting. Geostand Geoanal Res. doi:10.1111/j.1751-908X.2016.00379.x

Huber C, Bachmann O, Manga M (2009) Homogenization processes in silicic magma chambers by stirring and latent heat buffering. Earth Planet Sci Lett 283:38–47. doi:10.1016/j.epsl.2009.03.029

Huber C, Bachmann O, Dufek J (2011) Thermo-mechanical reactivation of locked crystal mushes: melting-induced internal fracturation and assimilation processes in magmas. Earth Planet Sci Lett 304:443–454. doi:10.1016/j.epsl.2011.02.022

Huber C, Bachmann O, Dufek J (2012) Crystal-poor vs. crystal-rich ignimbrites: a competition between stirring and reactivation. Geology 40:115–118. doi:10.1130/G32425.1

Jackson SE, Pearson NJ, Griffin WL, Belousova EA (2004) The application of laser ablation-inductively coupled plasma-mass spectrometry to in situ U–Pb zircon geochronology. Chem Geol 211(1):47–69. doi:10.1016/j.chemgeo.2004.06.017

Jaffey A, Flynn K, Glendenin L, Bentley Wt, Essling A (1971) Precision measurement of half-lives and specific activities of U 235 and U 238. Phys Rev C 4(5):1889. doi:10.1103/PhysRevC.4.1889

Johnson M, Rutherford M (1989) Experimentally determined conditions in the Fish Canyon Tuff, Colorado, magma chamber. J Petrol 30:711–737. doi:10.1093/petrology/30.3.711

Kaiser JF, de Silva S, Schmitt AK, Economos R, Sunagua M (2016) Million-year melt–presence in monotonous intermediate magma for a volcanic–plutonic assemblage in the Central Andes: contrasting histories of crystal-rich and crystal-poor super-sized silicic magmas. Earth Planet Sci Lett. doi:10.1016/j.epsl.2016.09.048

Klemetti EW, Clynne MAe (2014) Localized rejuvenation of a crystal mush recorded in zircon temporal and compositional variation at the Lassen Volcanic Center, Northern California. PLoS ONE 9(12):e113157. doi:10.1371/journal.pone.0113157

Liebske C (2015) iSpectra: an open source toolbox for the analysis of spectral images recorded on scanning electron microscopes. Microsc Microanal 21(04):1006–1016. doi:10.1017/S1431927615014336

Lipman PW (1967) Mineral and chemical variations within an ash-flow sheet from Aso caldera, South Western Japan. Contrib Mineral Petrol 16:300–327. doi:10.1007/BF00371528

Lipman PW (2000) The central San Juan caldera cluster: Regional volcanic framework. in PM Bethke and RL Hay, eds, Ancient Lake Creede: Its Volcano-Tectonic Setting, History of Sedimentation, and Relation of Mineralization in the Creede Mining District. Geol Soc Am Spec Pap 346:9–69. doi:10.1130/0-8137-2346-9.9

Lipman PW (2006) Geologic map of the central San Juan caldera cluster, southwestern Colorado. US Department of the Interior, US Geological Survey

Lipman PW (2007) Incremental assembly and prolonged consolidation of Cordilleran magma chambers: evidence from the Southern Rocky Mountain Volcanic Field. Geosphere 3(1):1–29. doi:10.1130/GES00061.1

Lipman PW, Bachmann O (2015) Ignimbrites to batholiths: Integrating perspectives from geological, geophysical, and geochronological data. Geosphere 11(3):705–743. doi:10.1130/GES01091.1

Lipman PW, McIntosh WC (2008) Eruptive and noneruptive calderas, northeastern San Juan Mountains, Colorado: Where did the ignimbrites come from? Geol Soc Am Mem 120(7–8):771–795. doi:10.1130/b26330.1

Lipman PW, Doe B, Hedge C (1978) Petrologic evolution of the San Juan volcanic field, Southwestern Colorado: Pb and Sr isotope evidence. Geol Soc Am Mem 89:59–82 doi:10.1130/0016-7606(1978)89<59:PEOTSJ>2.0.CO;2

Lipman PW, Dungan MA, Brown LL, Deino AL (1996) Recurrent eruption and subsidence at the Platoro Caldera complex, southeastern San Juan volcanic field, Colorado; new tales from old tuffs. Geol Soc Am Mem 108(8):1039–1055. doi:10.1130/0016-7606(1996)108<1039:REASAT>2.3.CO;2

Mahood GA (1990) Second reply to comment of R.S.J. Sparks, H.E. Huppert, and C.J.N. Wilson on "Evidence for long residence times of rhyolitic magma in the Long Valley magmatic system: the isotopic record in precaldera lavas of Glass Mountain". Earth Planet Sci Lett 99:395–399. doi:10.1016/0012-821X(90)90145-N

Marsh BD (1981) On the crystallinity, probability of occurrence, and rheology of lava and magma. Contrib Mineral Petrol 78:85–98. doi:10.1007/BF00371146

Martin VM, Morgan DJ, Jerram DA, Caddick MJ, Prior DJ, Davidson JP (2008) Bang! Month-Scale eruption triggering at Santorini Volcano. Science 321(5893):1178. doi:10.1126/science.1159584

Matthews N, Pyle D, Smith V, Wilson C, Huber C, van Hinsberg V (2012) Quartz zoning and the pre-eruptive evolution of the ~340-ka Whakamaru magma systems, New Zealand. Contrib Mineral Petrol 163(1):87–107. doi:10.1007/s00410-011-0660-1

Mattinson JM (2005) Zircon U–Pb chemical abrasion ("CA-TIMS") method: combined annealing and multi-step partial dissolution analysis for improved precision and accuracy of zircon ages. Chem Geol 220(1):47–66. doi:10.1016/j.chemgeo.2005.03.011

Miller CF, Wark DA (2008) Supervolcanoes and their explosive supereruptions. Elements 4:11–16. doi:10.2113/GSELEMENTS.4.1.11

Molloy C, Shane P, Nairn I (2008) Pre-eruption thermal rejuvenation and stirring of a partly crystalline rhyolite pluton revealed by the Earthquake Flat Pyroclastics deposits, New Zealand. J Geol Soc Lon 165:435–447. doi:10.1144/0016-76492007-071

Munoz JL (1984) F–OH and Cl–OH exchange in micas with applications to hydrothermal ore deposits. In: Bailey SW (ed) Reviews in Mineralogy and Geochemistry, vol 13. Mineralogical Society of America, Chantilly, VA, pp 469–493

Murphy M, Sparks R, Barclay J, Carroll M, Brewer T (2000) Remobilization of andesite magma by intrusion of mafic magma at the Soufriere Hills Volcano, Montserrat, West Indies. J Petrol 41(1):21–42. doi:10.1093/petrology/41.1.21

Pallister JS, Hoblitt RP, Meeker GP, Knight RJ, Siems DF (1996) Magma mixing at mount pinatubo: petrographic and chemical evidence from the 1991 Deposits. In: Newhall CG, Punongbayan RS (eds) Fire and mud: eruptions and lahars of Mount Pinatubo, Philippines, vol. Univ. Washington Press, Seattle, pp 687–731

Parat F, Dungan MA, Lipman PW (2005) Contemporaneous trachy-andesitic and calc-alkaline volcanism of the Huerto Andesite, San Juan Volcanic Field, Colorado, USA. J Petrol 46(5):859–891. doi:10.1093/petrology/egi003

Paton C, Hellstrom J, Paul B, Woodhead J, Hergt J (2011) Iolite: Freeware for the visualisation and processing of mass spectrometric data. J Anal At Spectrom 26(12):2508–2518. doi:10.1039/C1JA10172B

Petrus JA, Kamber BS (2012) VizualAge: a novel approach to laser ablation ICP-MS U-Pb geochronology data reduction. Geostand Geoanal Res 36(3):247–270. doi:10.1111/j.1751-908X.2012.00158.x

Putirka K (2008) Thermometers and barometers for volcanic systems. In: Putirka K, Tepley F (eds) Minerals, Inclusions and Volcanic Processes, vol 69. Reviews in Mineralogy and Geochemistry, Mineralogical Society of America, pp 61–120

Reid MR, Coath CD, Harrison TM, McKeegan KD (1997) Prolonged residence times for the youngest rhyolites associated with Long Valley Caldera; 230Th–238U ion microprobe dating of young zircons. Earth Planet Sci Lett 150(1–2):27–39. doi:10.1016/S0012-821X(97)00077-0

Riciputi LR (1991) Petrology and Nd, Sr and Pb isotopes of the central San Juan caldera cluster, Colorado. PhD Thesis. University of Wisconsin, Madison

Ruprecht P, Bachmann O (2010) Pre-eruptive reheating during magma mixing at Quizapu volcano and the implications for the explosiveness of silicic arc volcanoes. Geology 38:919–922. doi:10.1130/G31110.1

Ruprecht P, Bergantz GW, Dufek J (2008) Modeling of gas-driven magmatic overturn: tracking of phenocryst dispersal and gathering during magma mixing. Geochem Geophys Geosyst. doi:10.1029/2008GC002022

Ruprecht P, Bergantz GW, Cooper KM, Hildreth W (2012) The crustal magma storage system of Volcán Quizapu, Chile, and the effects of magma mixing on magma diversity. J Petrol. doi:10.1093/petrology/egs002

Scaillet B, Holtz F, Pichavant M (1998) Phase equilibrium constraints on the viscosity of silicic magmas 1. Volcanic-plutonic comparison. J Geophys Res 103(B11):27257–27266. doi:10.1029/98JB02469

Schärer U (1984) The effect of initial 230Th disequilibrium on young UPb ages: the Makalu case, Himalaya. Earth Planet Sci Lett 67(2):191–204. doi:10.1016/0012-821X(84)90114-6

Schmitt AK, Lindsay JM, de Silva S, Trumbull RB (2003) U-Pb zircon chronostratigraphy of early-Pliocene ignimbrites from La Pacana, north Chile: implications for the formation of stratified magma chambers. J Volcanol Geotherm Res 120(1–2):43–53. doi:10.1016/S0377-0273(02)00359-1

Schoene B, Schaltegger U, Brack P, Latkoczy C, Stracke A, Gunther D (2012) Rates of magma differentiation and emplacement in a ballooning pluton recorded by U–Pb TIMS-TEA, Adamello batholith, Italy. Earth Planet Sci Lett 355–356:162–173. doi:10.1016/j.epsl.2012.08.019

Simon JI, Renne PR, Mundil R (2008) Implications of pre-eruptive magmatic histories of zircons for U–Pb geochronology of silicic extrusions. Earth Planet Sci Lett 266(1–2):182–194. doi:10.1016/j.epsl.2007.11.014

Steven TA, Lipman PW (1976) Calderas of the San Juan volcanic field, southwestern Colorado. US Geol Surv Prof Pap 958:1–35

Storm S, Shane P, Schmitt A, Lindsay J (2012) Decoupled crystallization and eruption histories of the rhyolite magmatic system at Tarawera volcano revealed by zircon ages and growth rates. Contrib Mineral Petrol. doi:10.1007/s00410-011-0682-8

Sugawara T (2001) Ferric iron partitioning between plagioclase and silicate liquid: thermodynamics and petrological applications. Contrib Mineral Petrol 141(6):659–686. doi:10.1007/s004100100267

Tappa MJ, Coleman DS, Mills RD, Samperton KM (2011) The plutonic record of a silicic ignimbrite from the Latir volcanic field, New Mexico. Geochem Geophys Geosyst 12(10):Q10011. doi:10.1029/2011gc003700

Turner S, Costa F (2007) Measuring timescales of magmatic evolution. Elements 3:267–272. doi:10.2113/gselements.3.4.267

Vazquez JA, Reid MR (2004) Probing the accumulation history of the voluminous Toba Magma. Science 305:991–994. doi:10.1126/science.1096994

Walker GPL (1972) Crystal concentration in ignimbrites. Contrib Mineral Petrol 36:135–146. doi:10.1007/BF00371184

Walker BJ, Miller CF, Lowery LE, Wooden JL, Miller JS (2007) Geology and geochemistry of the Spirit Mountain batholith, southern Nevada: implications for timescales and physical processes of batholith construction. J Volcanol Geotherm Res 167:239–262. doi:10.1016/j.jvolgeores.2006.12.008

Waters LE, Lange RA (2015) An updated calibration of the plagioclase-liquid hygrometer-thermometer applicable to basalts through rhyolites. Am Mineral 100(10):2172–2184. doi:10.2138/am-2015-5232

Wolff JA et al (2015) Remelting of cumulates as a process for producing chemical zoning in silicic tuffs: a comparison of cool, wet and hot, dry rhyolitic magma systems. Lithos 236(2015):275–286. doi:10.1016/j.lithos.2015.09.002

Wotzlaw J-F, Schaltegger U, Frick DA, Dungan MA, Gerdes A, Gunther D (2013) Tracking the evolution of large-volume silicic magma reservoirs from assembly to supereruption. Geology 41:867–870. doi:10.1130/g34366.1

Zellmer GF, Blake S, Vance D, Hawkesworth C, Turner S (1999) Plagioclase residence times at two island arc volcanoes (Kameni Islands, Santorini and Soufrière, St. Vincent) determined by Sr diffusion systematics. Contrib Mineral Petrol 136:345–357. doi:10.1007/s004100050543

Zellmer G, Sparks R, Hawkesworth C, Wiedenbeck M (2003) Magma emplacement and remobilization timescales beneath Montserrat: insights from Sr and Ba zonation in plagioclase phenocrysts. J Petrol 44(8):1413–1431. doi:10.1093/petrology/44.8.1413

Zellmer GF, Sakamoto N, Hwang S-L, Matsuda N, Iizuka Y, Moebis A, Yurimoto H (2016) Inferring the effects of compositional boundary layers on crystal nucleation, growth textures, and mineral chemistry in natural volcanic tephras through submicron-resolution imaging. Front. Earth Sci 4:88. doi:10.3389/feart.2016.00088

Zielinsky RA, Lipman PW (1976) Trace-element variations at Summer Coon volcano, San Juan Mountains, Colorado, and the origin of continental-interior andesite. Geol Soc Am Mem 87:1477–1485   doi:10.1130/0016-7606(1976)87<1477:TVASCV>2.0.CO;2

Zimmerer MJ, McIntosh WC (2012) The geochronology of volcanic and plutonic rocks at the Questa caldera: constraints on the origin of caldera-related silicic magmas. Geol Soc Am Mem. doi:10.1130/b30544.1